International Journal of Image and Graphics, Vol. 1, No. 4 (2001) 659–680

GRADIENT-ORIENTED PROFILES FOR BOUNDARY PARAMETERIZATION AND THEIR APPLICATION TO CORE ATOMS TOWARDS SHAPE ANALYSIS

ROBERT J. TAMBURO*
Bioengineering, University of Pittsburgh,
3700 O'Hara Street Pittsburgh, PA 15261, USA
rjtst21@pitt.edu

GEORGE D. STETTEN
Visualization and Image Analysis Laboratory,
3700 O'Hara Street Pittsburgh, PA 15261, USA
george@stetten.com

Gradient-oriented profiles are presented as a novel method for boundary parameterization and unsupervised boundary classification. Each profile is created at locations of high gradient magnitude by sampling an ellipsoidal neighborhood of voxels oriented along the image gradient. Every profile is analyzed via nonlinear optimization to fit the best cumulative Gaussian, directly parameterizing the boundary to yield estimates of (1) extrapolated intensity values for voxels located far inside and outside of the boundary and (2) boundary location and width. For these parameter estimates, intrinsic measures of confidence are established to eliminate the low-confidence parameters. Gradient-oriented profiles are demonstrated on artificially generated three-dimensional test data and shown to accurately parameterize and classify the boundary, establishing them as a high-quality replacement for simpler methods of boundary detection. Towards shape analysis gradient-oriented profiles are applied to medial primitives known as core atoms. The additional intensity information delivered by gradient-oriented profiles improves the function of core atoms by eliminating dependence on the absolute direction of the local image gradient and the background intensity. The performance of core profiles is demonstrated on test data simulating a three-dimensional ultrasound scan of the heart improving the previous capabilities of core atoms.

Keywords: Core Profile; Boundary Parameterization; Core Atom.

1. Introduction

Boundary detection is a well-established field, described in practically any general reference.[1–4] Many methods of image analysis employ a boundary detection scheme that first begins with the identification of boundary candidates by simple measurement of the gradient magnitude throughout an image and selection of

*749 Benedum Hall, Department of Bioengineering, University of Pittsburgh, 3700 O'Hara Street, Pittsburgh, Pittsburgh, PA 15261, USA.

candidates above a pre-determined threshold. Such systems are sensitive to object and background intensity, as well as overall image contrast, for example the Roberts Cross and Sobel edge detectors. These issues may be overcome by providing a more detailed parameterization of the boundaries, which we accomplish with gradient-oriented profiles.

Boundaries in images are characterized by local changes in intensity values, corresponding to a strong gradient. Therefore, these boundaries can be found by taking the derivative of the image and locating the maximum derivatives. Taking the derivative of the image may proceed by convolving the image with a number of kernels, such as the Roberts Cross and Sobel kernels. The Roberts Cross convolution kernel when applied to gray-images yields gradient magnitude and location, but is very sensitive to noise. The Sobel convolution kernel is larger, effectively smoothing the image and reducing the high-frequency associated with noise. This makes the Sobel kernel better at detecting boundaries than the Roberts Cross, but it is slower to operate and still sensitive to noise.[5] We have followed the gradient boundary detection approach for the initial collection of boundary points. Gradient-oriented profiles begin by finding locations in the image with a gradient magnitude greater than a pre-determined threshold. This can be accomplished with any technique that delivers the gradient magnitude and orientation of the boundary point (we use a Difference of Gaussian (DoG) gradient detector).

The noise sensitivity of the Roberts Cross and Sobel kernel arise from taking a derivative, which amplifies the high-frequency noise in the image. Marr[6,7] and Canny[8] resolve this problem by convolving the image with a Gaussian kernel prior to calculating the derivative. Increasing the width of the Gaussian kernel smooths the image, reducing the detector's sensitivity to noise, but losing some of the finer details in the image. We also smooth the image with a Gaussian kernel prior to applying DoG gradient detector. After the Gaussian smoothing, Marr's approach proceeds with the application of a Laplacian of Gaussian (LoG) filter locating boundaries wherever its value is zero. The LoG can be closely approximated by a DoG and achieve the same accuracy if a slightly larger filter size is used. Canny's boundary detector requires a set of boundary detection filter masks that have various orientations. The masks contain a derivative of a Gaussian function to perform a directional derivative across the intended boundary. When applied, a smooth averaging profile appears in the mask along the intended boundary direction in order to reduce noise without compromising the sharpness of the boundary profile.[1] Like the Canny edge detector, we operate along the gradient direction averaging voxel intensities to reduce noise sensitivity and generate boundary profiles. The Marr and Canny edge detectors require multiple applications of filters at different scales for a thorough edge detection procedure. Gradient-oriented profiles require a single application for a full parameterization of the image boundaries.

A useful property of the gradient magnitude is its inherent insensitivity to rotation. More complex parameterizations of the boundary can also be made rotationally invariant by operating along the local gradient vector. *Steerable Filters*,

for example, parameterize the boundary using a basis set of Gaussian derivatives that is easily rotated into the coordinate system of the local boundary.[9] We accomplish an equivalent rotation with *gradient-oriented profiles* by projecting voxels onto the gradient vector to produce a one-dimensional intensity profile. Fitting a specific function to the profile, the cumulative Gaussian, directly yields physically significant estimates that parameterize the boundary; specifically, (1) the extrapolated intensity values for voxels located far inside and outside of the boundary and (2) estimates of boundary location and boundary width. Individual measures of confidence are calculated for these parameters to eliminate low-confidence parameters. However, initial oversampling for candidate boundary points results in a large population of overlapping neighborhoods. Thus, sufficient high-confidence parameter estimates remain for a thorough survey of the boundary.

The methodology of gradient-oriented profiles is presented in Sec. 2.1. Gradient-oriented profiles are applied to three-dimensional test data consisting of one boundary between two regions of differing intensities (Sec. 3.1). Unlike other boundary detectors that merely detect the presence of a boundary (not the actual location of the boundary), gradient-oriented profiles determine the optimal location of the true boundary and parameterize it supplying information useful to virtually all schemes of shape analysis. In Sec. 3.1.1 (Fig. 6), we compare the performance of the gradient-oriented profiles versus the DoG kernel for estimating the location of boundaries. Our application for this work is the automated parameterization of the left ventricular (LV) boundary and measurement of LV and myocardial volume in *real-time three-dimensional* (RT3D) ultrasound cardiac scans.[10] RT3D produces images that are 8-bit, three-dimensional, and anisotropic, although gradient-oriented profiles can be applied to any three-dimensional data. This imaging modality is capable of capturing volumes of cardiac data in real-time, but has a low signal-to-noise ratio. Automated detection of the LV and determination of its volume with time would be clinically useful in diagnosing abnormal cardiac function and calculating myocardial stress and strain. Such techniques could be generally applicable to all medical imaging modalities.

Deformable contours have been shown capable of finding and measuring the LV using data from 2D ultrasound scanners.[11–13] Coppini *et al.* have applied deformable surfaces to mechanically scanned 3D ultrasound data.[14] Stetten *et al.* have applied deformable methods to Real Time 3D (RT3D) ultrasound, but results were not encouraging due to the inherent low signal-to-noise ratio.[15] Further work by Stetten led to the development of an automatic technique that can successfully detect the LV and measure its volume in RT3D. A medial approach was taken relating multiple boundary points to common central points deep within the object by using *core atoms* as a construct to *medial node models*.[16]

A core atom is formed from pairs of boundary points that face each other across the intervening distance. This limits the shapes that can be found using core atoms, also making a measure of myocardial volume unfeasible. In addition, core atoms only use boundary point orientations, making it difficult to differentiate particular

tissue types on either side of the boundary. These limitations of core atoms can be overcome by providing intensity information about those tissues. Gradient-oriented profiles, do exactly this, thus it seems natural to apply gradient-oriented profiles to core atoms, enhancing their performance by (1) allowing the formation of core atoms by matching the intensities on the medial sides of both boundaries and (2) estimating the location of the anatomical boundary. The term *core profile* has been given to the newly constructed core atom enhanced by gradient-oriented profiles. The process of constructing core profiles is presented in Sec. 2.2 and the resulting performance of core profiles on three-dimensional test data resembling that of cardiac data can be found in Sec. 3.2. These results also include a simple and preliminary method for the measure of the volume in the test data corresponding to the LV and the myocardium.

2. Methods

2.1. *Construction and analysis of gradient-oriented profiles*

Our algorithm for boundary parameterization and classification proceeds in the following steps (described in corresponding subsections of the text):

(i) Find boundary candidates with a Difference of Gaussian (DoG) gradient detector;
(ii) Define ellipsoidal neighborhoods around detected boundary points and project voxels within each ellipsoid into bins along the major axis, yielding a profile of voxel intensity;
(iii) Fit a cumulative Gaussian to the intensity profile, estimating values for intensity on both sides of the boundary as well as location and width of the boundary;
(iv) Eliminate blatantly "bad" profiles;
(v) For the remaining profiles, calculate measures of confidence for the estimated values and eliminate those according to a certain threshold;
(vi) Classify the boundary using the high-confidence estimated values.

2.1.1. *Finding boundary candidates*

A population of candidate boundary points is collected on a regularized sampling grid using a Difference of Gaussian (DoG) gradient detector. There are many forms of DoG gradient detectors. One common version finds the difference between two concentric Gaussian kernels of different scale.[1] In contrast, our DoG consists of three pairs of same-scale Gaussian filters displaced in location along each of the cardinal axes from the sample point to measure the respective components of the gradient. We use our DoG gradient detector because it is more efficient and delivers gradient direction as well as gradient magnitude. Each boundary candidate that exceeds a pre-determined threshold for gradient magnitude is used to generate an individual boundary profile.

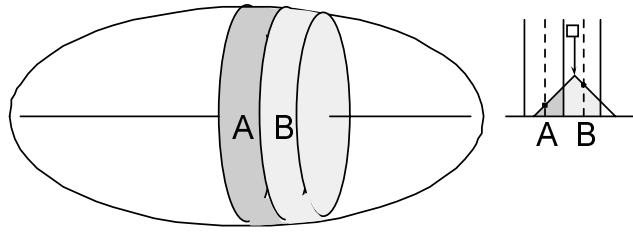

Fig. 1. The left shows an ellipsoidal neighborhood; whose center is the location of the DoG gradient detector and major axis is the gradient vector, with two adjoining disks, A and B. The right shows a voxel (square) projecting onto the major axis, splatting 3/4 of its intensity value into bin B and 1/4 into bin A.

2.1.2. *Generating a boundary profile*

Given the detection of a boundary by the DoG detector, a boundary profile is generated in the direction of the gradient by sampling the voxels in an ellipsoidal neighborhood centered at the DoG detector whose major axis is along the gradient vector. We project the voxels within the ellipsoidal neighborhood onto the major axis where their values are *splatted* into bins. Splatting is a technique commonly used in computer graphics that projects the footprints of individual voxels onto a plane. Overlapping footprints are collected in bins to form a rendered image. Instead of splatting onto a plane, we splat onto a line, namely, the major axis of the ellipsoid. As shown in Fig. 1, the ellipsoid is divided into disks along the major axis, with corresponding bins collecting footprints from voxels in adjoining disks. Since the footprints are wider than the bins, each voxel contributes to a number of bins. We use a triangular footprint, with the effect of linearly interpolating the intensity of each voxel between neighboring bins along the axis. The weight of contribution for each voxel is separately stored so that the total intensity in each bin can be normalized. Thus, the profile represents the average voxel intensity for each disk within the ellipsoidal sampling region. Averaging within each disk reduces the effect of image noise on the boundary profile.

2.1.3. *Fitting the profile and estimating parameter values*

A number of different functions could potentially be used to fit to the profile. The cumulative Gaussian was chosen for reasons now described. Most anatomical boundaries are very abrupt, inherently step functions at the sub-millimeter scale where one tissue ends and another begins. Image acquisition is inevitably limited in resolution, however, with a particular device exhibiting an overall "point spread function" usually at a significantly larger scale than the actual tissue boundary. Additional blurring may be performed intentionally or inevitably, for example, during the image processing that converts the raw data to an image. The result of these sequential convolutions tends to have the effect of convolution with a Gaussian kernel because of the Central Limit Theorem. Thus we can expect the step function of

the anatomical boundary to reach the image analysis stage as a cumulative Gaussian, i.e., the convolution of a step function with a Gaussian. Therefore, by fitting a cumulative Gaussian, we may, in effect, reverse the blurring and parameterize the original boundary.

Fitting a cumulative Gaussian to a boundary profile requires optimizing four parameters: (1) standard deviation, corresponding to the boundary width, (2) mean, corresponding to boundary location, and (3, 4) two asymptotic values, corresponding to voxel intensity on either side of the boundary sufficiently far from the boundary to be unaffected by blurring.

The cumulative Gaussian is derived as follows. The normalized Gaussian

$$G(x) = \frac{1}{\sigma\sqrt{2\pi}}\, e^{-(x-\mu)^2/2\sigma^2}\,, \tag{1}$$

is integrated to yield the error function (erf)

$$\int_{-x}^{x} G(v)\, dv = erf\left(\frac{x-\mu}{\sigma\sqrt{2}}\right), \tag{2}$$

which is scaled and offset to yield the cumulative Gaussian $C(x)$

$$C(x) = I_1 + \frac{I_2 - I_1}{2}\left(1 + erf\left(\frac{x-\mu}{\sigma\sqrt{2}}\right)\right). \tag{3}$$

The four fixed parameters of $C(x)$ are μ (mean), σ (standard deviation), and I_1 and I_2 (asymptotic voxel intensity inside and out). On one side of the boundary

$$erf(-\infty) = -1\,, \quad C(-\infty) = I_1 \tag{4}$$

and on the other side

$$erf(\infty) = 1\,, \quad C(\infty) = I_2\,. \tag{5}$$

The four parameters are labeled in Fig. 2, which shows a particular fit of the cumulative Gaussian along the sampled portion of the boundary profile.

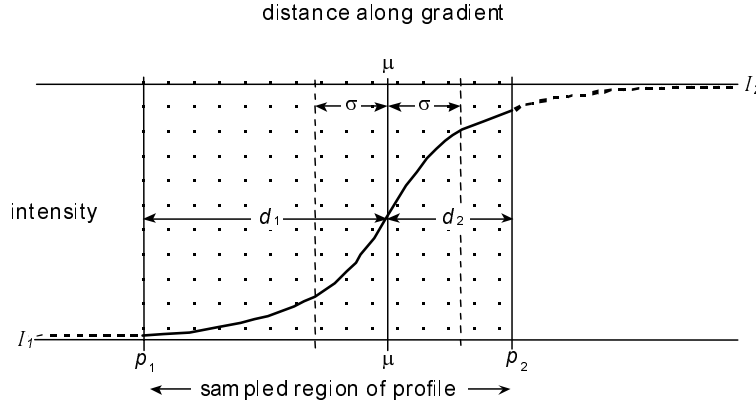

Fig. 2. A cumulative Gaussian fit to a profile from a sampled region (shaded area).

A variety of techniques are available for optimizing the fit of a nonlinear function to a set of sample points. We chose a Quasi-Newton nonlinear optimization algorithm provided as part of the *AD Model Builder* from Otter Research, Inc.,[17] because it does not require explicit derivation of derivatives and is acceptably rapid and robust. To make intelligent use of parameters estimated from the curve fitting, measures of confidence for each of the parameters are established. This takes the form of two steps, as described in the following two sections.

2.1.4. *Eliminating bad profiles*

The first step involves the elimination of unacceptable parameters by rejecting blatantly "bad" profiles for which a reasonable fit of the cumulative Gaussian could not be found. The fit is rejected if:

(i) Either extrapolated voxel intensity value I_1 or I_2 falls outside of the acceptable range of values for the imaging modality;
(ii) The estimated boundary location μ falls outside of the ellipsoidal sample region.

Boundary profiles that are rejected by these criteria are no longer considered. Determining confidence levels for the estimated parameters and eliminating low-confidence estimates on a parameter-by-parameter basis further eliminates bad profiles.

2.1.5. *Establishing intrinsic measures of confidence*

If a fit was accepted for a given profile, the next step is to determine a measure of confidence in the individual parameters of the cumulative Gaussian. We postulate that the confidence for a particular parameter is related to the location of the boundary within the ellipsoid, as well as the boundary width.

In Fig. 2, the cumulative Gaussian that best fits an intensity profile is shown. By definition, the underlying function (ignoring the particular region over which it was sampled) is symmetrically distributed on either side of the mean μ (μ with representing the optimum boundary location). However, the function is not generally symmetrically distributed with respect to the sampling region, represented by the shaded area from p_1 to p_2. Given that the best fit has a mean μ and standard deviation σ, two distances d_1 and d_2 can be defined from μ to p_1 and p_2 respectively, from which two normalized distances z_1 and z_2 can be computed as

$$z_1 = \frac{d_1}{\sigma} \quad \text{and} \quad z_2 \frac{d_2}{\sigma}\,. \tag{6}$$

The values of z_1 and z_2 indicate how many standard deviations from μ in each direction the actual samples extend, and serve as measures of confidence for I_1 and I_2, respectively. For each direction, the greater the number of standard deviations the samples extend from μ, the less the effect of the boundary and the more accurately we can expect to estimate intensity. For example, in Fig. 2 we have more

confidence in the estimate I_1 than the estimate I_2, because $d_1 > d_2$, and therefore $z_1 > z_2$.

In addition to a measure of confidence for I_1 and I_2, we have developed one for μ. Our measure of confidence for μ determines whether sufficient samples exist on either side of μ to estimate it accurately. We define this measure of confidence as

$$z_{\min} = \min(z_1, z_2)\,. \tag{7}$$

If on either side of μ, insufficient samples exist to anchor the cumulative Gaussian, $z_{\min}$ will be small, and we can expect difficulty in estimating μ accurately. Like the measures of confidence for profile intensity estimates, a threshold is also placed on $z_{\min}$ to determine whether there is acceptable confidence in μ.

2.1.6. *Classifying the boundary*

Armed with high-confidence estimates for I_1, I_2 and μ, we can now classify the local boundary in terms of these parameters. The parameters I_1 and I_2 estimate voxel intensity beyond the ellipsoid, sufficiently far from the boundary to be stable and the mean μ estimates the anatomical boundary location within the ellipsoid.

Rather than struggling to extract the last bit of classification from each profile, our measures of confidence permit us to exclude individual parameters on a case-by-case basis. In the initial gathering of boundary candidates, we use a sampling interval well below the conventional Nyquist guidelines, to yield a comprehensive set of profiles from which a thorough examination of a given boundary can be made. By setting thresholds for the intrinsic measures of confidence, we may reject or accept individual estimates to make intelligent use of this over-sampled population. The exact method of setting these thresholds optimally is beyond the scope of this paper.

2.2. *Core profiles*

The theory behind the construction of core profiles is very similar to that of core atoms. A brief review will be included here, but a more detailed explanation can be found elsewhere.[18,19] Rather than consisting of two boundary points like a core atom, a core profile consists of two boundary profiles. The collection of the boundary profiles follows the methods as discussed in Sec. 2.1. For each boundary profile, search regions are established along the image gradient in both directions. Within these two regions, boundary profiles are sought after that meet the following requirements:

(i) The distance between the boundary profiles (optimal boundary locations) is within a specified range. This permits savings in computation if there is *a priori* information about the expected width of the object. If this requirement is met, in addition to those that follow, a core profile is create and this distance

is termed the scale of the core profile and is defined as

$$\|\vec{s}_{1,2}\| = b_2 - b_1\,, \quad \text{where} \quad s_{\min} \leq \|\vec{s}_{1,2}\| \leq s_{\max}\,. \tag{8}$$

The vector $\vec{s}_{1,2}$ indicates the direction from the first boundary profile to the second boundary profile and the core profile is located at the midpoint between the two boundary profiles. Figure 3 illustrates a core profile created across an object of intensity I_1 against a background of intensity I_2.

(ii) The face-to-faceness, defined as

$$F(b_1, b_2) = \left| \left(\frac{\vec{s}_{1,2}}{\|\vec{s}_{1,2}\|} \cdot \vec{n}_1 \right) \left(\frac{\vec{s}_{1,2}}{\|\vec{s}_{1,2}\|} \cdot \vec{n}_2 \right) \right|, \tag{9}$$

where $\vec{n}_i\,(i = 1, 2)$ is the orientation of the ith boundary profile, is sufficiently close to one, while still allowing some variation in the relative orientations of the boundaries.

(iii) For the candidate boundary profiles, the intensity estimates for the space they traverse must both be high-confidence estimates (established in Sec. 2.1.5) and have similar values within some pre-determined threshold. As illustrated in Fig. 3, $I_{ij}\,(i, j = 1, 2)$ is the intensity estimate for region i by core profile b_j. The threshold placed on this intensity estimate is denoted $z_{ij}\,(i, j = 1, 2)$, the threshold of core profile b_j's intensity estimate for region i. Thus, core profile $\vec{s}_{1,2}$ is acceptable if all of the following are met:

$$\text{(a)} \quad z_{11} > \mathit{threshold}(z_{11}) \tag{10}$$

$$\text{(b)} \quad z_{12} > \mathit{threshold}(z_{12}) \tag{11}$$

$$\text{(c)} \quad |I_{11} - I_{12}| < \tau, \text{ where } \tau \text{ is an intensity threshold} \tag{12}$$

Any profile may link to multiple profiles becoming involved in multiple core profiles. The additional intensity information delivered by gradient-oriented profiles

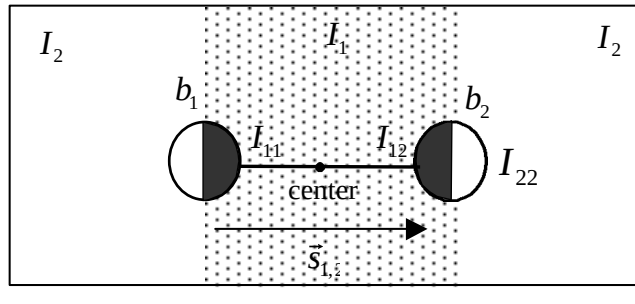

Fig. 3. A core profile spanning across data containing voxels of intensity I_1 (shaded area) against a background of intensity I_2. The core profile consists of two boundary profiles in the direction of $\vec{s}_{1,2}$ and a center midway between the optimal boundary locations. I_{ij} is an intensity estimate for region i by core profile b_j. The angle between the core vector $\vec{s}_{1,2}$ and the individual gradient directions does not have to be zero (see (ii) of requirements). Also, the exterior voxel intensities I_2 do not have be the same for each boundary profile (see (iii) of requirements).

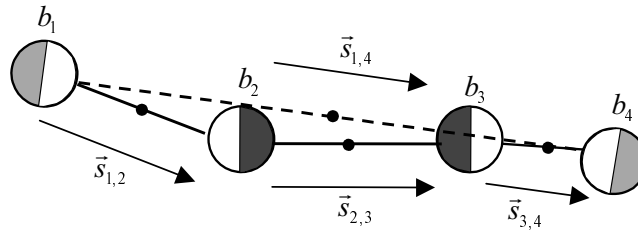

Fig. 4. A network consisting of four core profiles formed in data consisting of at least three different values for voxel intensity. The core profiles indicated with the solid lines are termed homogeneous core profiles and the dashed line represents a heterogeneous core profile because it spans regions of intensity non-specific to its estimates.

permits core profiles to be formed in both directions of the gradient resulting in a network of core profiles as shown in Fig. 4. Core profiles $\vec{s}_{1,2}$, $\vec{s}_{2,3}$ and $\vec{s}_{3,4}$ are termed homogeneous core profiles because their entire lengths span local regions for which the gradient-oriented profiles estimate. Core profile $\vec{s}_{1,4}$ is a *heterogeneous* core profile because it spans regions that include homogeneous core profiles. This may prove to be useful in constructing a hierarchy of objects within a dataset for analysis or compression.

The third criterion for core profile construction includes only high-confidence estimates for the shared intensities of the profiles. In certain cases, this constraint can be extended to impose that both intensity estimates for each core profile are high-confidence estimates. This would be useful in classifying boundaries where both intensity regions are known to be in a certain range and a deviation from this intensity range would imply that an abnormality exists in that region.

3. Results

3.1. *Gradient-oriented profile test data*

We demonstrate the application of gradient-oriented profiles on a 3D data set, 100 voxels on a side, consisting of 8-bit voxels. An artificial sphere was generated with a radius of 30 voxels, an interior value of 64, and an exterior value of 128. A binomial kernel was applied multiple times to the data, approximating a Gaussian and simulating the point-spread function of a real image. Using the DoG gradient detector kernel, as described in Sec. 2.1.1, a total of 1,400 boundary candidates was found. According to the method described in Sec. 2.1.2, voxels in an ellipsoidal neighborhood were sampled for each boundary candidate. The center of the ellipsoid was the location of the DoG kernel. The major axis of the ellipsoid along the gradient had a length of ten voxels and the minor axes had lengths of six voxels each. Along the major axis, ten bins were established, each being one voxel wide. The intensity values of the voxels within the ellipsoid were splatted into the bins (using a triangle footprint), and normalized by the splatting weights. A cumulative Gaussian was fit to the resulting intensity profile as described in Sec. 2.1.3.

Of the resulting 1,400 profiles, 240 profiles were eliminated because they did not meet the constraints defined in Sec. 2.1.4. For the remaining profiles, the measures of confidence for the classification parameters were calculated as derived in Sec. 2.1.5. The results of applying gradient-oriented profiles to the 3D test model were compared to the known parameters of the test data and described below.

3.1.1. *Measuring accuracy of gradient-oriented profiles in the test model*

After eliminating "bad" profiles, the accuracy of the remaining profile parameters was measured using *a priori* knowledge of the test data. The test data contains a sphere, which is completely parameterized by its radius (the distance R_{true} from its center to the location of the boundary) and the intensities on both sides of the boundary. The interior intensity of the sphere is denoted I_1, and the exterior, I_2. The estimate of intensity derived from the profile for either I_1 or I_2 is denoted I_{estimate}, and we define I_{error} as

$$I_{\text{error}} = |I_{\text{true}} - I_{\text{estimate}}|\,, \tag{13}$$

where I_{true} is the known voxel intensity I_1 (64 inside the sphere) or I_2 (128 outside the sphere).

Figure 5 shows that profiles with μ near the center of the ellipsoid are able to estimate the intensity on either side of the boundary better than when μ is located away from the center of the ellipsoid. When μ is located away from the centers of the ellipsoid, intensity values are estimated less accurately in that direction.

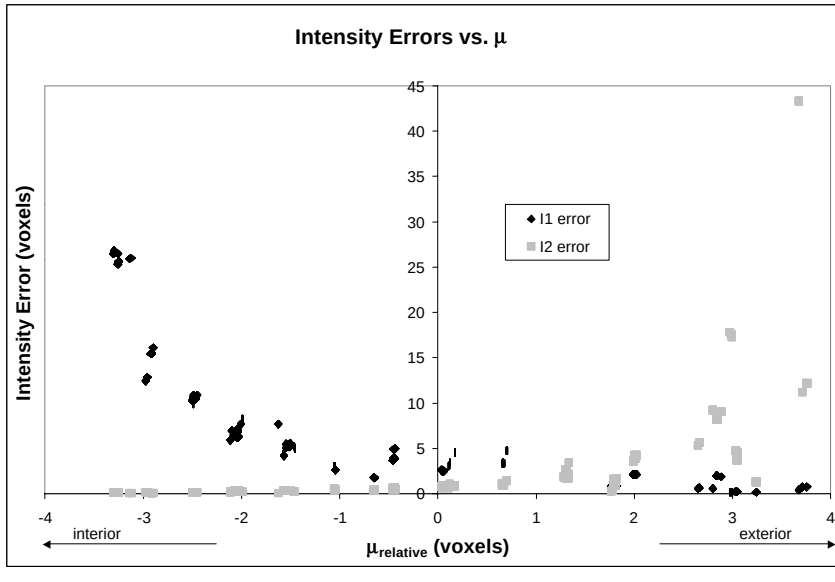

Fig. 5. The distribution of error in estimating the intensity values on either side of the boundary as a function of μ (with zero being the center of the ellipsoid).

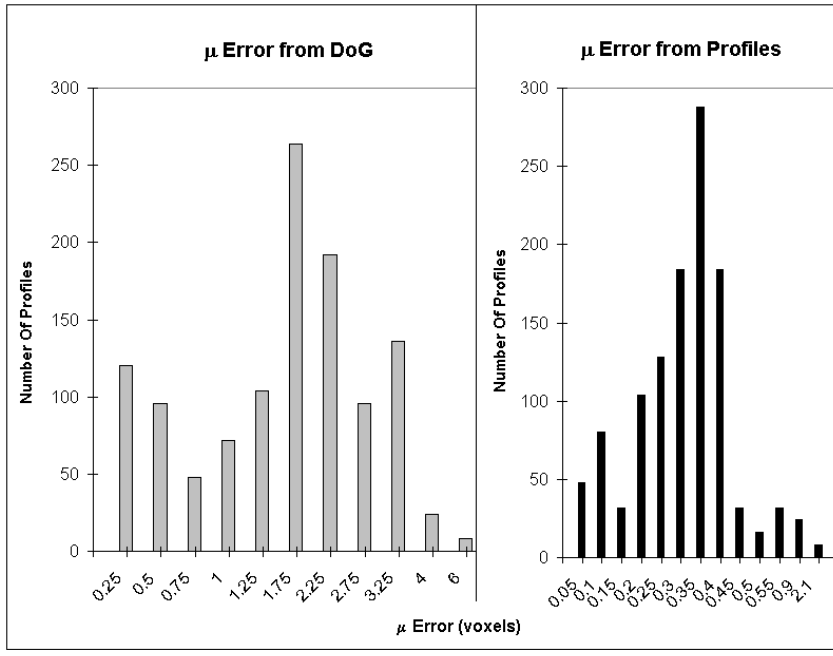

Fig. 6. Accuracy in estimating the location of the boundary by gradient-oriented profiles compared to the location of the DoG kernel.

However, such a profile will estimate the intensity in the opposite direction with high accuracy. For example, in Fig. 5, I_2 can be estimated to within one unit of intensity, when μ is much less than zero.

The accuracy in estimating the true boundary location of the test data was determined as follows. The distance from the center of the sphere to the location on the major axis of the ellipsoid corresponding to μ was defined as the estimated radius R_{estimate}. This was compared to the known radius R_{true} of the sphere, with R_{error} being defined as

$$R_{\text{error}} = |R_{\text{true}} - R_{\text{estimate}}| \,. \tag{14}$$

Figure 6 shows that boundary profiles are more accurate in determining the true location of the boundary than the original DoG boundary kernels. Out of the 1,160 total profiles, 1,152 (99.31%) had location estimates within one voxel.

3.1.2. *Judging intrinsic measures of confidence*

We have shown that gradient-oriented profiles are able to estimate the intensity values and localize the boundary location. We now demonstrate the validity of our intrinsic measures of confidence.

The measures of confidence for the profile parameters were calculated using the methods discussed in Sec. 2.5. Figure 7 shows the error in estimating I_1 (interior of

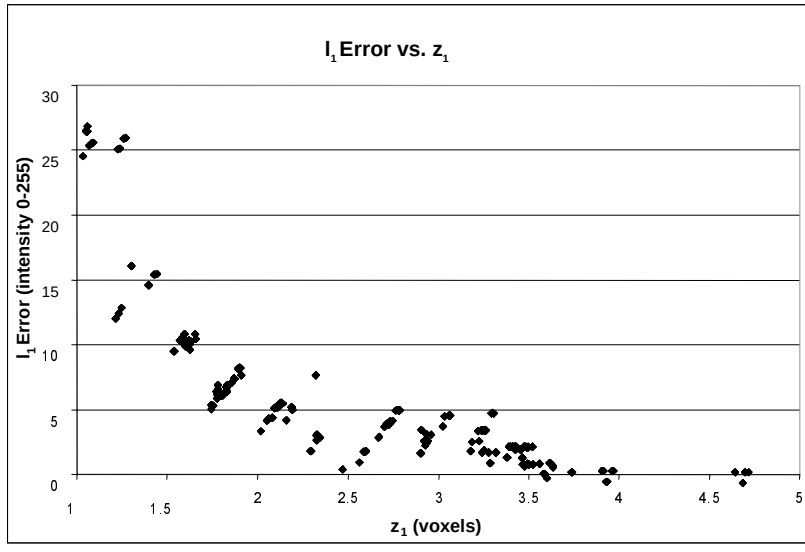

Fig. 7. The error in estimating the intensity for the interior of the sphere I_1 versus its measure of confidence Z_1.

sphere) as a function of its measure of confidence z_1. For two standard deviations ($z_1 \leq 2.0$) the error, $I_{\text{error}} < 5$. Therefore, as seen in Fig. 7, a threshold placed on z_1 of 2.0 would guarantee this accuracy.

With this threshold, 776 of the total profiles (67%) will estimate the intensity I_1 with high confidence. Similarly, Fig. 8 shows the error in estimating I_2 (exterior of

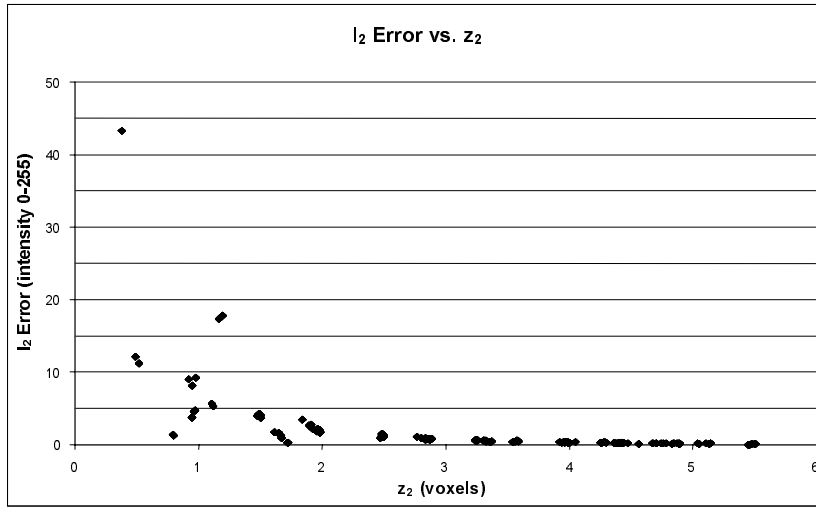

Fig. 8. The error in estimating the intensity exterior to the sphere I_2 as a function of its measure of confidence Z_2.

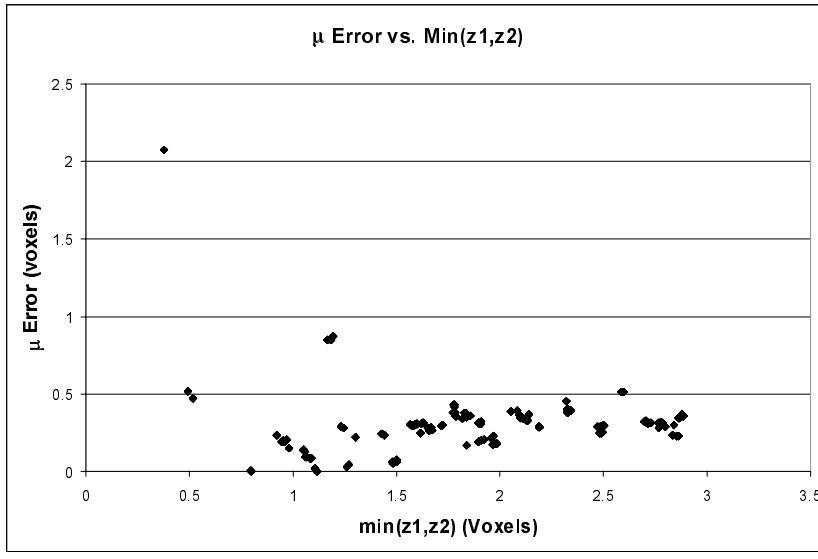

Fig. 9. Error in boundary location from gradient-oriented profiles versus measure of confidence.

sphere) as a function of its the measure of confidence z_2, with similar results using a threshold for z_2 of 1.45.

We predicted earlier that profiles with μ near the center of the ellipsoid should be able to estimate both intensities I_1 and I_2 with high accuracy. We identified 632 out of the 1,160 (54.48%) profiles that were able to reliably classify both intensities as described above. Our measure of confidence for μ is shown in Fig. 9. For $z_{\min} > 1/2$ standard deviations a high confidence seems warranted for μ, since it is consistently within one voxel of the true boundary. This threshold places high confidence in the estimates of boundary location for 1,152 out of 1,160 profiles (99.31%).

3.2. *Core profile test data*

Core profiles were tested on a 3D data set, 100 voxels cubed, consisting of 8-bit voxels. The test target was chosen to simulate an ultrasound scan of a heart. It consisted of an artificial sphere generated with a radius of 15 voxels within another sphere of radius 30 voxels. The interior of the smaller sphere had a value of 32 (left ventricular cavity) and an exterior value of 128 and this boundary will be called the inner boundary. The larger sphere shared the same voxels as the exterior of the smaller sphere creating a shell (myocardium) of value 128 and the exterior had a value of 64 (background). This boundary will be called the outer boundary. This test data is shown in Fig. 10(a).

Using the DoG gradient detector kernel, as described in Sec. 2.1.1, a total of 1,936 boundary candidates were found. The parameters for the size of the ellipsoid, bin size, and footprint type were the same as in Sec. 3.1. Of the resulting 1,936

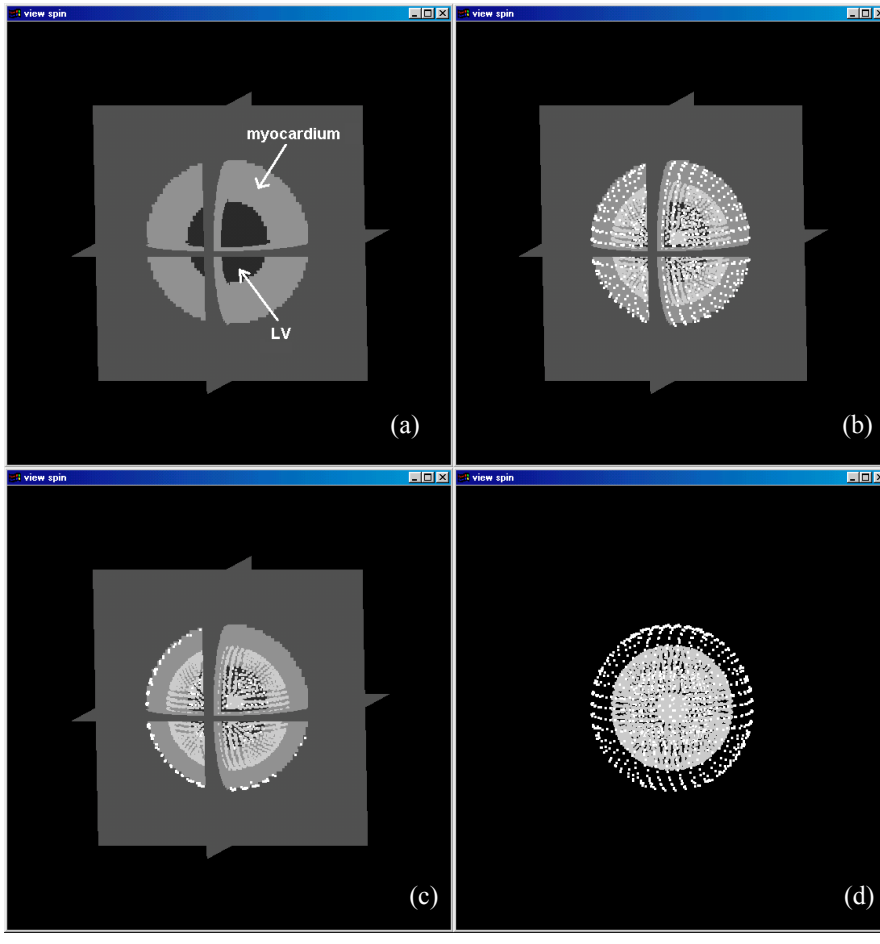

Fig. 10. (a) Test data simulating a 3D ultrasound image of a heart. The smaller sphere is filled with voxels of intensity 32 (LV), the ring is filled with voxels of intensity 128 (myocardium), and the background is of voxel intensity 64. (b) The results of applying core profiles to the test data overlaid on the data. The white dots correspond to the optimal boundary points for the core profiles. The light gray dots represent the centers of the core profiles. (c) A cut-away view exposing the centers of the core profiles. (d) The resulting core profiles without the test data.

profiles, 384 profiles were eliminated because they did not meet the constraints defined in Sec. 2.1.4, leaving 1,552 profiles for analysis. In Figs. 10(b)–10(d), the optimal boundary locations found by the profiles are indicated by the white dots. For the remaining profiles, the measures of confidence for the classification parameters were calculated as derived in Sec. 2.5. There were a total of 98,771 boundary comparisons and 10,110 met the requirements as discussed in Sec. 2.2.1 for core profile formation. Figures 10(b)–10(d) show the core profiles by the location of their centers, indicated by the light gray dots. The analysis of these core profiles can be found in Sec. 3.2.2. Also, the accuracy of the gradient-oriented profiles for this new

test model is also measured to ensure that they perform in an effective, consistent manner. These results are described below.

3.2.1. *Measuring the accuracy of gradient-oriented profiles in the new test model*

Unlike the previous test data, the new test model contains two boundaries. However, the accuracy of the gradient-oriented profiles can be carried out the same way as discussed in Sec. 3.1.1 if the population of the profiles is separated by their estimation of the radius of the boundary. There were 280 profiles near the inner boundary, and 1,263 profiles near the outer boundary. Figure 11 shows the distribution of error in estimating the intensity values on either side of both boundaries as a function of μ. Results are consistent with previous results showing that when μ is near the center of the ellipsoid, profiles are able to estimate the intensity on either side of the boundary better than when μ is located away from the center of the ellipsoid.

From Eq. (14), the accuracy of the profiles in estimating the true boundary location can be measured. Out of the 1,152 profiles, 1,488 (95.87%) were able to estimate the location of a boundary within one voxel. The DoG detector had only 456 out of the 1,152 (29.38%) boundary points within one voxel of a boundary. Figure 12 shows the error of all of the profiles in estimating the true location of the boundaries as well as the error in estimating the true location of the boundaries with the DoG detector.

The measures of confidence for the profiles parameters were calculated using the methods described in Sec. 2.1.5. Plotting I_1 versus z_1 for the inner boundary shows the error in estimating the inner intensity of the inner boundary. When z_1 is greater than 1.9, the error in estimating I_1 is less than 7. With this threshold, 80% of the inner boundary profiles can estimate I_1 with high confidence. Plotting I_1

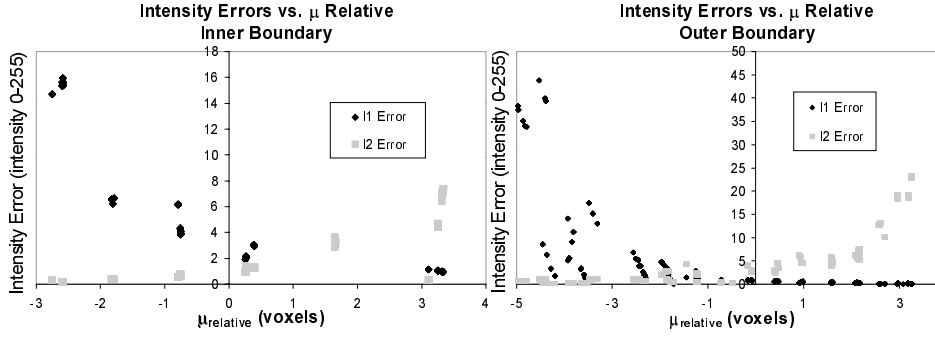

Fig. 11. Both graphs show the error in estimating intensities on either side of a boundary as a function of μ. The center of the ellipsoid is zero. The left graph shows the error in estimating the intensities on both sides of the inner boundary. The right graph shows the error in estimating the intensities on both sides of the outer boundary.

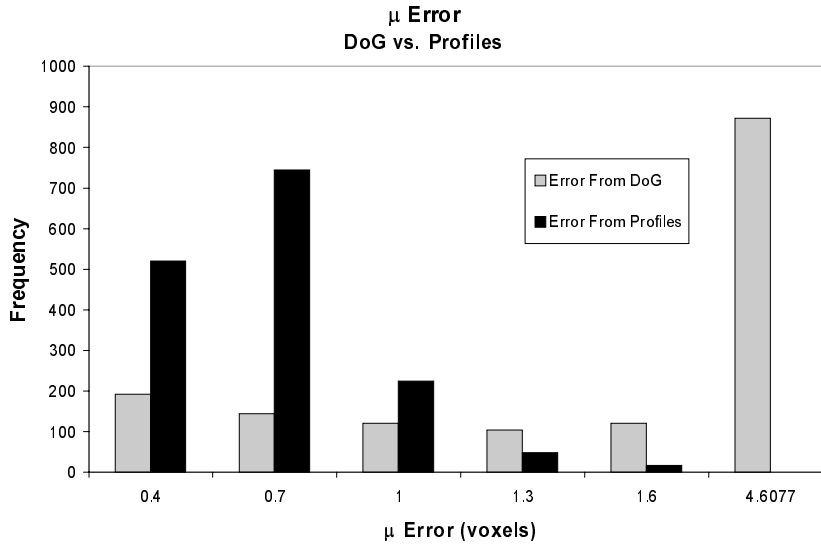

Fig. 12. Comparison of errors in estimating boundary locations with the DoG detector versus gradient-oriented profiles. 95.87% of the total profiles as opposed to 29.38% of the total DoG kernels can estimate a boundary location within one voxel.

versus z_2 shows the error in estimating the outer intensity of the inner boundary. If an intensity error of 8 is acceptable for estimating I_1, 100% of the inner boundary profiles can estimate I_1 with high confidence.

Similarly for the outer boundary, plotting I_1 versus z_1 shows the error in estimating the inner intensity. A threshold of 1.1 on z_1 accepts profile estimates (84%) of the inner intensity of the outer boundary I_1 to within 7. Plotting I_1 versus z_2 shows the error in estimating the outer intensity of the outer boundary. A threshold of 1.6 on z_2 permits 84% of the outer boundary profiles to estimate, with high-confidence, the outer intensity I_2.

3.2.2. *Analysis of core profile population*

Recall that core profiles can be described by two profiles its center point and its scale. In the previous section, it was shown that the profiles composing core profiles are able to accurately locate the true boundaries and estimate the intensities of the test model for an ultrasound image of a heart. We now show that the center point and scale of the core profiles created are consistent with the expected results. The spherical nature of the data simplifies this analysis. The radius of a core profile is defined as the distance from the center point of the core profile to the center of the spheres. The center points of the core profiles should be near the center of the two spheres or centered in the slab between the two spheres. Figure 13 shows the radii of the core profiles, where the center of the spheres is zero and the midpoint of the slab is 22.5 on the graph.

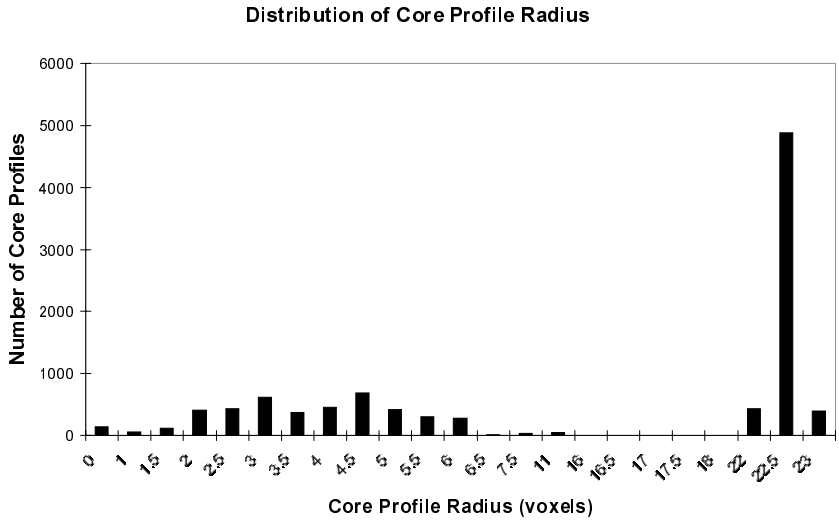

Fig. 13. The distribution of center points of the core profiles. The center of the spheres is at 0 and the center of the slab between the spheres is at 22.5.

Many core profiles have their centers located very close to the midpoint of the slab, but there is a significant spread for the centers of core profiles formed across the spheres. This spread is expected because the gradients are not directed towards the center of the spheres and the large scale of these core profiles. Core profiles formed across the spheres should have a scale of either 30 or 60 voxels. Those formed across the slab should have a scale near 15 voxels. Figure 14 shows that there are these three populations of core profiles.

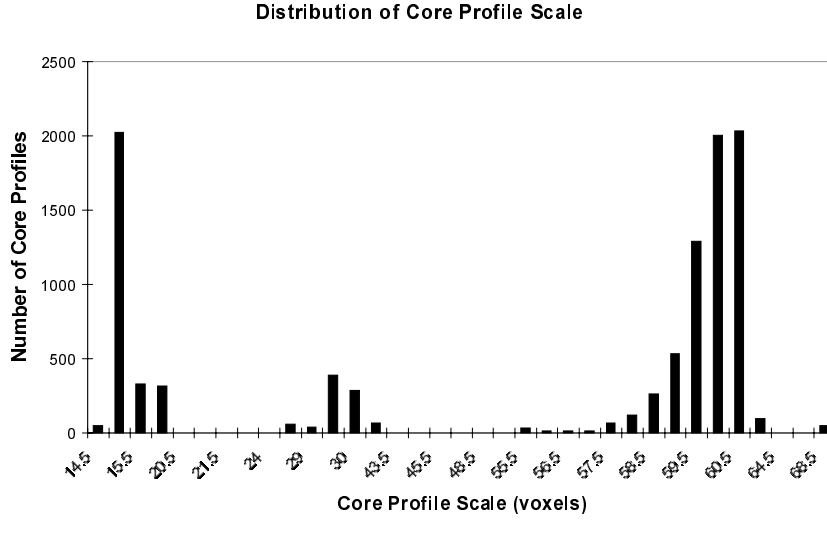

Fig. 14. Distribution of core profile scale consistent with expected results.

Table 1. An average core profile scale after sorting them by scale permits the calculation of LV and myocardial volume. The true are found simply by using the equation of a sphere and the known radii of the data.

Method of Calculation	LV Volume (voxels^3)	Heart Volume (voxels^3)	Myocardium Volume (voxels^3)
Known Parameters of Data	14,137.18	113,097.50	98,960.28
Average Core Profile Scale	13,215.80	111,002.80	97,787.05
Percent Error	6.5175%	1.8520%	1.1856%

3.2.3. *Measures of volume*

The volume in the test data corresponding to the LV and myocardium can be calculated with the known radii of the spheres making up the test data with the equation for the volume of a sphere,

$$V = \frac{4}{3}\pi r^3 . \tag{15}$$

The volume of the LV is calculated using Eq. (15) with a radius of 15 voxels. Likewise, the volume of the heart (LV and myocardium) is found with Eq. (15) and a radius of 30 voxels. The volume of the myocardium is the difference between LV volume and the heart volume. This is taken as the true volume measure because two sphere radii parameterize this test model.

These volume measures are calculated using the scale of the core profiles. The core profiles with a scale between 20 and 45 voxels are averaged and used to approximate the volume of the LV using Eq. (15). Similarly, the heart volume is found with core profiles having a scale between 45 and 70 voxels and the volume of the myocardium is the difference between these two measures. Table 1 contains a summary of these volume measures as well as an error measure (percent error) for the volume calculated by the core profiles.

The volume measures found with average core profile scale were very accurate compared to the known volumes. Calculating the volumes in this manner was possible because the radii of the spheres were known. In real data, volumes cannot be calculated in this manner. Currently, more practical methods of volume calculation are being developed based on labeling voxels according to the probability of being within the region of interest and summing the weights of the voxels for a count of the voxels within this region without explicitly defining a surface.

4. Conclusion

We have presented gradient-oriented profiles, a method of unsupervised boundary parameterization suitable for classification. By operating along the direction of the gradient vector, gradient-oriented profiles are insensitive to rotation. The cumulative Gaussian provides estimates that parameterize the boundary by estimating (1) extrapolated intensity values for voxels located far inside and outside of the boundary, (2) anatomical boundary location, and (3) (although not yet validated) blurred boundary width. Intrinsic measures of confidence have been shown to be

capable of eliminating inaccurate parameter estimates. Thresholds placed on these measures of confidence would allow classification of boundaries with high confidence. Gradient-oriented profiles have proven capable of accurately parameterizing the boundary in our test data.

To further demonstrate the application of gradient-oriented profiles to classification, they will be applied to data containing noise. Also, more investigation is warranted into the effects of (1) using neighborhoods with shapes other than an ellipsoid, (2) using footprints with shapes other than a triangle, (3) altering bin size along the gradient, and (4) altering relative size of the sampling neighborhood compared to the DoG gradient kernel.

Gradient-oriented profiles have been applied to core atoms to enhance their performance by (1) allowing the formation of core atoms by matching the intensities on the medial sides of both boundaries, and (2) estimating the location of the anatomical boundary. This newly constructed core atom is called a core profile. Core profiles were applied to test data simulating 3D cardiac ultrasound data. The performance of the gradient-oriented profiles used to construct the resulting core profiles was tested with this new data demonstrating that profiles can parameterize multiple boundaries accurately. The performance of the core profiles was consistent of expected results quantified by analyzing their center points and scales and comparing them to the quantities calculated from the known parameters of the test data. Core profiles were also shown to accurately measure the volumes of the simulated LV and myocardium moving closer towards automated parameterization of the LV boundary and measures of LV and myocardial volume in RT3D ultrasound cardiac scans.

Acknowledgments

This work was funded by grants from the Whitaker Foundation and the National Library of Medicine Insight Toolkit (ITK) project.

References

1. P. Mlsna and J. Rodriguez, "Gradient and laplacian-type edge detection," *From Handbook of Video and Image Processing*, ed. Al Bovik, 415 (2000).
2. M. Petrou and P. Bosdogianni, *Image Processing*: *The Fundamentals* (John Wiley and Sons, New York, 1999).
3. W. Pratt, *Digital Image Processing* (John Wiley annd Sons, New York, 1991).
4. A. Jain, *Fundamentals of Digital Image Processing*, ed. T. Kailath (Prentice Hall, New Jersey, 1989).
5. S. E. Umbaugh, *Computer Vision and Image Processing*: *A Practical Approach Using CVIP Tools* (Prentice Hall, New York, 1997).
6. D. Marr and E. Hildreth, "Theory of edge detection," *Proc. Royal Society* **207**, 187 (1980).
7. D. Marr, *Vision* (W. H. Freeman & Co., 1982).
8. J. Canny, "A computational approach to edge detection," *IEEE Pattern Analysis and Machine Intelligence* **8**, 679 (1986).

9. W. Freeman and E. Adelson, "The design and use of steerable filters," *IEEE Trans. Pattern Analysis and Machine Intelligence* **13**, 891 (1991).
10. G. Stetten, T. Ota, C. Ohazama, C. Fleishman, J. Castelucci, J. Oxaal, T. Ryan, J. Kisslo, and O. v. Ramm, "Real-Time 3D ultrasound: A new look at the heart," *J. Cardiovascular Diagnosis and Procedures* **15**, 73 (1998).
11. V. Chalana, D. T. Linker, D. R. Haynor, and Y. Kim, "A multiple active contour model for cardiac boundary detection on echocardiographic sequence," *IEEE Trans. Medical Image* **15**, 290 (1996).
12. S. Malassiotis and M. G. Strintzis, "Tracking the left ventricle in echocardiographic images by learning heart dynamics," *IEEE Trans. Medical Imaging* **18**, 282 (1999).
13. I. A. Hunter, J. J. Soraghan, J. Christie, and T. S. Durrani, *Detection of Echocardiographic Left Ventricle Boundaries Using Neural Networks* (*Computers in Cardiology*, London, UK) 201 (1993).
14. G. Coppini, R. Poli, and G. Valli, "Recovery of the 3-D shape of the left ventricle from echocardiographic images," *IEEE Trans. Medical Imaging* **14**, 301 (1995).
15. G. Stetten, T. Irvine, D. Ritscher, O. T. v. Ramm, J. Panza, V. Sachdev, J. Castellucci, M. Jones, and D. Sahn, *Improved Accuracy for a Semi-Automated Method for Computing Right Ventricle (RV) Cavity Volumes From Real-Time 3D Echo*: *Comparison Studies to Ultrasonic Crystals in An Open-Chest Animal Model* (*American College of Cardiology 48th Scientific Sessions*, New Orleans) (1999), in press.
16. G. Stetten and S. M. Pizer, "Medial-node models to identify and measure objects in Real-Time 3D echocardiography," *IEEE Trans. Medical Imaging* **18**, 1025 (1999).
17. Otter Research, Ltd, AD Model Builder. http://otter-rsch.com/admodel.htm.
18. G. D. Stetten and S. M. Pizer, "Medial node models to identify and measure objects in Real-Time 3D echocardiography," *IEEE Trans. Medical Imaging* **18**, 1025 (1999).
19. G. Stetten, "Automated identification and measurement of cardiac anatomy via analysis of medial primitives," Doctoral Dissertation, *Dept. Biomedical Eng.* (University of North Carolina, Chapel Hill 1999) http://www.stetten.com/george/publications/phd.

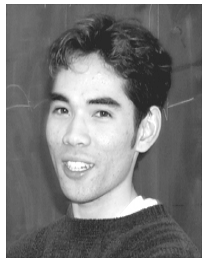

Robert Tamburo received his B.S. from Delaware State University in 1999 with a double major in Physics with in Engineering Emphasis and Mathematics. He is currently enrolled as a Ph.D. candidate in the Department of Bioengineering at University of Pittsburgh.

In 1996, he interned in the Department of Physics at the University of Delaware and studied the affects of magnetic annealing on permanent magnetic alloys. In 1997, he interned in the Department of Biomedical Imaging at Mayo Graduate School and segmented the paranasal sinuses from the Visible Human Female project. In 1998, he interned in the Department of Bioengineering at the University of Virginia and quantitatively modeled the abdominal skin flap vasculature of a rat.

George Stetten received his B.S. in Engineering and Applied Physics from Harvard University in 1976. After working in the future MIT Media Lab and at the Woods Hole Oceanographic Institute, he received an M.S. degree in Neurobiology/Computing from New York University in 1986, and an M.D. degree from the SUNY Syracuse in 1991. He earned his doctoral degree in 2000 in Biomedical Engineering at the University of North Carolina, Chapel Hill while maintaining faculty status at Duke University. Dr. Stetten is currently an Assistant Professor in Bioengineering at the University of Pittsburgh and a Research Scientist at the Robotics Institute at Carnegie Mellon University. His research involves a new method of identifying, measuring, and visualizing anatomical structures in 3D image data, based on local properties of shape. He has also developed a system for merging ultrasound images with human vision to guide invasive procedures, and is a founding member of the National Library of Medicine Insight Toolkit Consortium to produce a standard computing environment for medical image analysis.